

FIELDS: Face reconstruction with accurate Inference of Expression using Learning with Direct Supervision

Chen Ling¹ Henglin Shi^{1,2} Hedvig Kjellström¹

¹ KTH Royal Institute of Technology, Sweden, {chenlin,hedvig}@kth.se

² Linköping University, Sweden, henglin.shi@liu.se

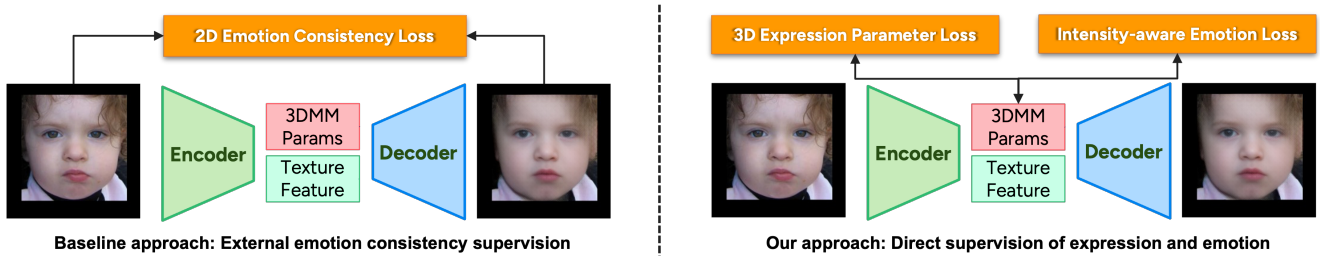


Figure 1. Comparison between the baseline approach, which relies on external emotion consistency losses, and our FIELDS framework, which introduces direct 3D expression parameter supervision from scan data alongside an integrated emotion-recognition branch.

Abstract

Facial expressions convey the bulk of emotional information in human communication, yet existing 3D face reconstruction methods often miss subtle affective details due to reliance on 2D supervision and lack of 3D ground truth. We propose FIELDS (Face reconstruction with accurate Inference of Expression using Learning with Direct Supervision) to address these limitations by extending self-supervised 2D image consistency cues with direct 3D expression parameter supervision and an auxiliary emotion recognition branch. Our encoder is guided by authentic expression parameters from spontaneous 4D facial scans, while an intensity-aware emotion loss encourages the 3D expression parameters to capture genuine emotion content without exaggeration. This dual-supervision strategy bridges the 2D/3D domain gap and mitigates expression-intensity bias, yielding high-fidelity 3D reconstructions that preserve subtle emotional cues. From a single image, FIELDS produces emotion-rich face models with highly realistic expressions, significantly improving in-the-wild facial expression recognition performance without sacrificing naturalness.

1. Introduction

In interpersonal communication, nonverbal signals which includes facial/body cues convey far more emotional con-

tent than spoken words [14, 39]. With the rise of deep learning [24, 30, 56], facial expression recognition (FER) has become a fundamental pillar of affective computing [64], enabling systems to map visible facial movements to internal emotional states [29]. Precise FER is indispensable in emotion-aware applications such as social robots [17], driver fatigue detection [26], and in-clinic pain assessment [45]. Consequently, extracting accurate, geometry-aware facial expression representations is essential for capturing latent emotional signals in muscle movements and enabling dependable emotion recognition.

In order to extract such geometry-aware expression representations, we propose FIELDS (Face reconstruction with accurate Inference of Expression using Learning with Direct Supervision) as illustrated in Fig. 1, a hybrid 2D/3D supervision framework that not only enforces image-level consistency but also directly teaches the encoder true 3D expression signals and aligns its outputs with affective targets – yielding 3D facial representations that faithfully capture both geometric nuance and genuine emotional content.

We build on the deep learning paradigm, in which the deep encoder first regresses the 3D Morphable Models (3DMM) [3, 13] parameters – in our case, the FLAME model [31] – from a single image and a differentiable renderer or an image-to-image synthesizer as the decoder then generates the corresponding face [51, 53]. The encoder-decoder reconstruction framework is driven by

self-supervised consistency between the input and synthesized images, indirectly optimizing the geometry encoder [8, 9, 16, 34, 47, 49]. Recent advances focus on refining expression fidelity through three key innovations: external emotion-consistency losses (EMOCA [8]), enhanced neural rendering with alternating optimization to avoid encoder masking (SMIRK [47]), and improved texture extraction via multi-scale appearance tokenizer (TEASER [34]).

However, the self-supervised 3DMM reconstruction pipeline is fundamentally limited by the absence of unified 3D expression ground truth: existing spontaneous 3D + emotion datasets either lack consistent mesh topology or do not provide 3DMM-compatible parameters. As a result, methods must rely solely on 2D cues, leading to two critical issues. First, 2D consistency losses cause the decoder to compensate for encoder errors rather than improve its geometry predictions, and the inherent 2D/3D domain gap prevents the encoder from learning precise, emotion-rich representations. Second, introducing a 2D emotion-consistency loss can over-emphasize expression intensity: as SMIRK [47] demonstrates, heavier emotion-loss weighting leads to exaggerated, less natural reconstructions. While this “intensity enhancement” [66] may boost discrete emotion-classification accuracy, it is less suited for continuous affective modeling, *e.g.* with valence–arousal (VA) [15, 48], which requires sensitivity to subtle expression variations.

To address these limitations, FIELDS extends the self-supervised paradigm with two complementary supervision signals. First, we align reconstructed expression parameters with authentic 3D labels obtained by fitting the 3DMM to spontaneous-expression scans from BP4D [63], providing direct 3D parameters guidance. Second, we add an auxiliary emotion-recognition module that predicts affective labels from the 3D expression parameters; during training, an intensity-aware emotion loss jointly optimizes this branch

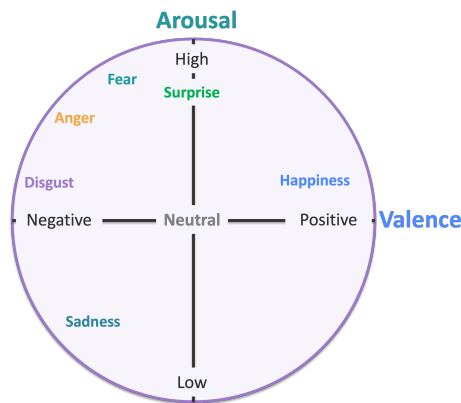


Figure 2. A circumplex model of affect [15, 48] with discrete emotions [14] overlaid. Adapted from [57].

and the geometry encoder, encouraging reconstructions that are both faithful to real muscle deformations and rich in genuine affective content. This dual-supervision strategy yields 3D expression representations that improve downstream FER performance without sacrificing geometric accuracy or naturalness.

In summary, our contributions are threefold:

- Hybrid 2D/3D Supervision: we augment the 2D self-supervision with direct FLAME expression parameter supervision, enabling the encoder to learn from both image-based consistency and limited ground-truth 3D data.
- Dataset Alignment with BP4D: we fit FLAME to spontaneous 4D scans of BP4D to obtain authentic expression parameters, which we use to directly supervise our expression regression encoder.
- Auxiliary Emotion Supervision: we add a parallel emotion recognition head on the predicted 3D expression parameters, using an intensity-aware loss to constrain exaggeration and preserve genuine affective detail.

2. Related Work

2.1. Facial Representation in Emotion Analysis

Emotion analysis from images is typically defined according to one of two annotation methods [24, 30, 56]: *discrete* categories, most often the six universal emotions of *Anger, Fear, Happiness, Surprise, Disgust, Sadness* as defined by Paul Ekman [14], or the *continuous* valence-arousal space. As shown in Fig. 2, valence denotes the hedonic tone of affect (negative to positive), whereas arousal indexes the level of activation or energy (low to high). Discrete emotion labels map to prototypical regions in the valence–arousal plane, whereas the circumplex’s continuous labels explicitly encode affect intensity and gradation – information absent from categorical classes. Both methods are widely used in benchmarks and downstream applications, and they motivate representations that are sensitive to subtle, muscle-driven facial deformations [15, 48].

Early FER relied on handcrafted 2D geometry cues – sparse landmarks [37], contour shapes [58], and optical flow [38] – to approximate muscle motion. Later, dense 3D observations such as 2.5D depth maps [65], laser-scan meshes [42], and point clouds [41] provided finer deformation detail but were costly to acquire and often dataset-specific. These signals improved fidelity but are costly and, without explicit structure, often conflate person-specific geometry with expression.

The 3D Morphable Models (3DMM) [3, 13, 31, 43] have demonstrated an ability to disentangle identity-related face shape geometry and emotion-relevant expression detail, thus providing rich, geometry-aware representations that go beyond the limitations of purely 2D or image space features. Recent works leverage 3DMM parameters or inter-

mediate 3D features for emotion recognition and valence-arousal regression from images [2, 6, 8, 12, 28, 44, 47, 52], demonstrating that 3D facial representations are predictive for affect while being more robust to pose and illumination than 2D appearance alone. At the same time, prior studies note that aggressively weighting emotion losses can inflate expressions and introduce artifacts, raising questions about *naturalness* despite higher scores. We follow this 3DMM-based line but focus on preserving emotion-rich yet natural expressions.

2.2. Monocular 3DMM-based Face Reconstruction

In this review we focus on monocular 3DMM-based reconstruction for FER-ready facial codes. For a survey of model-free pipelines, *e.g.* using direct mesh, voxels or implicit regression, see [11, 51].

Within 3DMM methods, optimization-based fitting via analysis-by-synthesis is interpretable yet slow and sensitive to occlusions and initialization [4, 21, 27, 46], whereas learning-based regressors and neural rendering improve speed and realism but can trade geometric semantics for pixel fidelity and blur identity-expression boundaries.

We organize learning-based work by the supervision they employ: sparse [10, 16, 23] or dense [1, 59] keypoints and contours [33] calibrate coarse geometry but suffer from sparsity and detector noise; photometric terms [10, 16, 20, 50, 61] impact all parameters but are fragile to misalignment and rendering quality; perceptual losses [62] align with human judgment yet are hard to balance and may exaggerate expressions [8, 47]; identity features or multi-image constraints [10, 16, 20, 60] strengthen subject consistency but risk biasing identity shape; explicit 3D supervision [6, 23, 54, 60] (meshes or 3DMM parameters) offers accurate targets but inherits the biases of the pseudo ground truth. Motivated by these trade-offs, we adopt a hybrid supervision scheme that combines a unified 2D consistency objective with direct parameter-space constraints on 3DMM codes, including expression supervision and intensity-aware emotion losses, so that categories anchor where to deform while valence-arousal calibrate how much to deform.

In this line, EMOCA [8] was the first to introduce an external emotion-consistency loss via a pretrained affect classifier, explicitly encouraging affect preservation. SMIRK [47] augments this with a neural renderer and alternating optimization to prevent the renderer from masking encoder errors. TEASER [34] further improves expression detail by replacing hand-crafted texture priors with a novel multi-scale appearance tokenizer, indirectly sharpening geometry estimation without explicit emotion losses. Our framework continues this 3DMM thread and unifies these ideas with hybrid 2D/3D supervision.

3. Method

We present a hybrid 2D/3D supervision framework FIELDS that extends the TEASER [34] self-supervised 3D face reconstruction with two key innovations: direct FLAME [31]-expression supervision from BP4D [63] scans and an auxiliary emotion-recognition head, yielding high-fidelity, affect-rich 3D reconstructions. As shown in Fig. 3, our model comprises: (1) a FLAME-based encoder and neural generator for disentangled shape, pose and expression estimation; (2) direct 3D expression loss using ground-truth FLAME parameters; and (3) an emotion recognition head with an intensity-aware loss.

3.1. Architecture

FLAME Model. We leverage the FLAME model to parameterize 3D facial geometry as identity shape $\beta \in \mathbb{R}^{300}$, expression $\psi \in \mathbb{R}^{100}$ and pose $\theta \in \mathbb{R}^{3k+3}$, where k represents rotations around 4 joints (neck, jaw, left eyeball, right eyeball) and the last 3 dimensions are the global head rotation. Given $\{\beta, \psi, \theta\}$, FLAME generates the 3D face mesh $V \in \mathbb{R}^{5023 \times 3}$. To adapt FLAME for face reconstruction, with the extension of eye closure blendshapes [67] $\psi_{eye} \in \mathbb{R}^2$ and the subsection of $\{\psi, \theta\}$, we formally define our FLAME model as follows:

$$V = \text{FLAME}(\beta, \Psi, \theta_{head} \in \mathbb{R}^3), \quad (1)$$

where $\Psi = \{\psi_{exp} \in \mathbb{R}^{50}, \psi_{eye}, \theta_{jaw} \in \mathbb{R}^3\}$ succinctly aggregates a group of parameters governing expression-related geometry and $\theta_{head} \in \mathbb{R}^3$ is the full head rotation.

Encoder. Following the notation of SMIRK [47] and TEASER [34], the image encoder $E(I)$ is separated into four different branches, three geometry encoders $E_\beta(I)$, $E_\Psi(I)$, $E_\Theta(I)$ and one token encoder $E_T(I)$.

Given the input image I , geometry encoders output the FLAME parameters, as well as the camera parameters $c \in \mathbb{R}^3$, here we group the global transformation parameters as $\Theta = \{c, \theta_{head}\}$. Consequently, the geometry encoders are formally defined as:

$$E_\beta(I) = \beta, E_\Psi(I) = \Psi, E_\Theta(I) = \Theta. \quad (2)$$

For appearance features, the multi-level CNN features $\{x_i\}_{i=1}^K$ are extracted from different stages of the token encoder E_T , pool and project each via $z_i = F_i(P(x_i))$, $i = 1, \dots, K$, then form the appearance token by channel-wise concatenation:

$$E_T(I) = [z_1 \odot z_2 \odot \dots \odot z_K] = T, \quad (3)$$

here P is average pooling, F_i a fully connected layer, and \odot denotes concatenation. This yields a single appearance token T that fuses both high-level semantics and fine-grained textures.

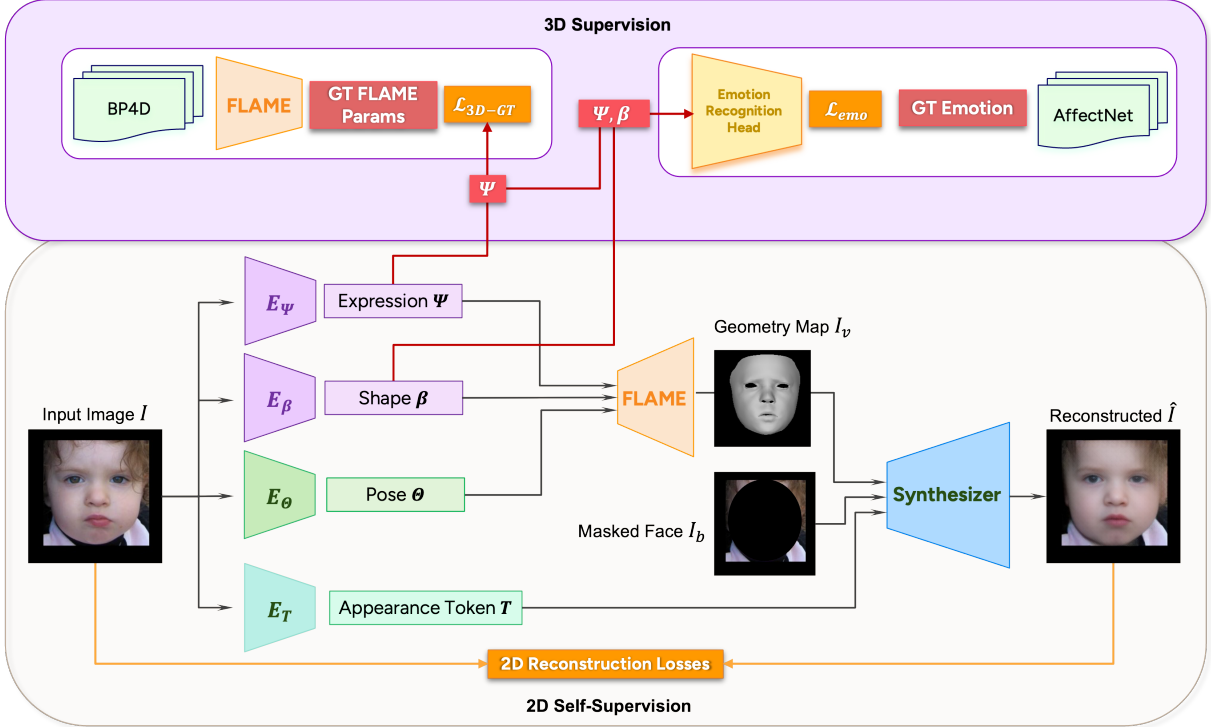


Figure 3. Illustration of the FIELDS pipeline. Given an input image I , encoders predict FLAME parameters (shape β , expression Ψ , pose Θ) and an appearance token T ; FLAME produces geometry maps that, together with I_b and T , are fused by a synthesizer to generate \hat{I} . Besides the inherited 2D consistency losses (gray box), we add 3D supervision (purple box): (i) BP4D provides fitted FLAME targets for an expression parameter loss \mathcal{L}_{3D-GT} , and (ii) AffectNet supplies labels for an auxiliary emotion head trained with \mathcal{L}_{emo} on (Ψ, β) . Initialization: the FLAME parameter encoders are pretrained, the token encoder and synthesizer are initialized from TEASER [34], and the emotion head is randomly initialized. During training we freeze only the pose encoder E_θ and update the remaining components jointly.

Neural Synthesizer. We adopt TEASER’s Token-guided Face Synthesizer [34] as our neural synthesizer G^* . It ingests three inputs: 1. the rasterized geometry map I_v , which is the monochrome rendering of the reconstructed face mesh V and generated by a neural rasterization renderer; 2. the masked background I_b , which applies a mask function $M(I)$ to crop the face out and convey the background information; 3. the multi-scale appearance token T . It produces the final image \hat{I} via a lightweight U-Net structure model:

$$\hat{I} = G^*(I_v \odot I_b \odot T). \quad (4)$$

This design ensures strict geometric alignment (through I_v), preserves background consistency (through I_b), and injects rich semantic information of appearance details (through T).

Emotion Recognition Head. Given the encoder predicted FLAME parameters $\hat{\beta}, \hat{\Psi}$, we employ a lightweight 4-layer Multi-Layer Perceptron (MLP) with BatchNormalization and LeakyReLU activations to jointly predict continuous valence–arousal and discrete emotion categories:

$$[\hat{v}, \hat{a}, \hat{\mathbf{p}}] = \text{MLP}_{emo}(\hat{\beta}, \hat{\Psi}), \quad (5)$$

where $\hat{v}, \hat{a} \in \mathbb{R}$ are the regressed valence-arousal scores, and $\hat{\mathbf{p}} \in \Delta^C$ is the softmax probability over C emotion classes.

3.2. Optimization of Hybrid 2D/3D Supervision

3.2.1. 3D Expression Supervision

FLAME Expression Ground Truth. We leverage the publicly available BP4D [63] 4D scan dataset by fitting each scan sequence to the FLAME model using the standard fitting pipeline [32]. This process yields expression parameters ground truth ψ_{expr} for a wide range of spontaneous expressions under naturalistic conditions.

3D Facial Expression Loss. To directly supervise the expression encoder, we apply a mean squared error (MSE) loss between the predicted expression parameters $\hat{\psi}_{\text{expr}}$ and the ground truth ψ_{expr} :

$$\mathcal{L}_{3D-GT} = \|\hat{\psi}_{\text{expr}} - \psi_{\text{expr}}\|_2^2. \quad (6)$$

This loss encourages the encoder to produce FLAME expression parameters that closely match those obtained from high-fidelity 3D scans.

3.2.2. Auxiliary Emotion Supervision

Intensity-Aware Emotion Loss. We train this emotion recognition head using a combination of regression and classification losses:

$$\mathcal{L}_{\text{emo}} = \lambda_r (v - \hat{v})^2 + \lambda_r (a - \hat{a})^2 + \lambda_c \text{CE}(\mathbf{p}, \hat{\mathbf{p}}), \quad (7)$$

where (v, a) are the ground-truth valence–arousal labels, \mathbf{p} is the discrete class label, CE denotes cross-entropy, and λ_r, λ_c balance the regression and classification terms.

The joint regression–classification objective ties *magnitude* (via (v, a)) and *category* (via \mathbf{p}): the categorical term shapes discriminative boundaries in the expression–code space, while the VA regressors act as an amplitude regularizer, encouraging calibrated (non-exaggerated) deformations and reducing the tendency to gain classification accuracy by inflating facial motions.

3.2.3. 2D Consistency Supervision

2D Consistency Loss. Following SMIRK [47] and TEASER [34], both the encoder and synthesizer leverage a unified 2D consistency loss, denoted $\mathcal{L}_{2\text{D-cons}}$, which combines several pixel-, perceptual- and landmark-based terms. Concretely, it includes a **photometric loss** $\mathcal{L}_{\text{photo}} = \|I - \hat{I}\|_1$, a **perceptual (VGG) loss** $\mathcal{L}_{\text{perc}} = \|\Gamma(I) - \Gamma(\hat{I})\|_1$ with $\Gamma(\cdot)$ the VGG feature extractor, and a **standard landmark loss** $\mathcal{L}_{\text{lmk}} = \sum_{i=1}^K \|\mathbf{k}_i - \mathbf{k}'_i\|_2^2$, where \mathbf{k}_i are the detected 2D landmarks and \mathbf{k}'_i their projections from the reconstructed mesh. To handle yaw variations θ_y , a **pose-dependent landmark loss** $\mathcal{L}_{\text{pdl}} = \|M_L(\theta_y) L - M_L(\theta_y) L_v\|_2^2$ is also applied, with $M_L(\theta_y)$ being the visibility mask. Finally, it focuses on expression-sensitive regions by parsing mouth and eye masks M_m and M_e and computing a **region loss** $\mathcal{L}_{\text{rg}} = \|(M_m + M_e) \odot I - (M_m + M_e) \odot \hat{I}\|_2^2$. For compactness, fixed per-term weights are applied via a coefficient vector \mathbf{w} denoted:

$$\mathcal{L}_{2\text{D-cons}} = \langle \mathbf{w}_{2\text{D}}, (\mathcal{L}_{\text{photo}}, \mathcal{L}_{\text{perc}}, \mathcal{L}_{\text{lmk}}, \mathcal{L}_{\text{pdl}}, \mathcal{L}_{\text{rg}}) \rangle. \quad (8)$$

This unified loss is then used in Eqs. (10) and (11).

3.2.4. Regularization

Before hybrid training, we pretrain the geometry encoders as base model B by aligning their predictions to the shape estimates of MICA [67], which provides a stable initialization of the parameter manifold.

We further adopt the frozen base model B for parameter-space regularization: the encoder’s predicted parameters are constrained to be close to the corresponding outputs of B . Let $[B(I)]_\beta, [B(I)]_{\psi_{\text{expr}}}$ denote the base model’s shape and expression parameters for image I . We define the **shape regularizer** as $\text{Reg}_{\text{shape}} = \|\hat{\beta} - \text{sg}([B(I)]_\beta)\|_2^2$ and the **expression regularizer** as $\text{Reg}_{\text{expr}} = \|\hat{\psi}_{\text{expr}} -$

$\text{sg}([B(I)]_{\psi_{\text{expr}}})\|_2^2$, where $\text{sg}(\cdot)$ indicates stop-gradient on the base model outputs (i.e., gradients do not flow into B).

With the hyperparameters $\lambda_{\text{shape-reg}}$ and $\lambda_{\text{expr-reg}}$ that weights the shape- and expression-regularization terms, the total regularizer is:

$$\mathcal{L}_{\text{reg}} = \lambda_{\text{shape-reg}} \text{Reg}_{\text{shape}} + \lambda_{\text{expr-reg}} \text{Reg}_{\text{expr}}. \quad (9)$$

3.3. Training Procedure

We alternate two steps per iteration – an Encoder Pass and a Synthesizer Pass – to prevent one component from compensating the other’s errors.

Encoder Pass. We freeze the pretrained shape/pose and appearance-token encoders, and optimize only the expression encoder with

$$\mathcal{L}_E = \lambda_{2\text{D}} \mathcal{L}_{2\text{D-cons}} + \lambda_{3\text{D}} \mathcal{L}_{3\text{D-GT}} + \lambda_{\text{emo}} \mathcal{L}_{\text{emo}} + \mathcal{L}_{\text{reg}}. \quad (10)$$

Synthesizer Pass. We freeze all encoders and update only the synthesizer with

$$\mathcal{L}_{G^*} = \lambda_{2\text{D}} \mathcal{L}_{2\text{D-cons}} + \lambda_{\text{exp}} \mathcal{L}_{\text{cyc}} + \lambda_{\text{tok}} \mathcal{L}_{\text{tok-cyc}}. \quad (11)$$

Here \mathcal{L}_{cyc} enforces cycle consistency on expression parameters recovered from the rendered image, and $\mathcal{L}_{\text{tok-cyc}}$ preserves appearance tokens across render–reencode.

Alternating Eqs. (10) and (11) yields emotion-aligned, identity-stable 3DMM parameters while avoiding appearance compensation in the synthesizer.

4. Experiments

4.1. Dataset

We train on six public datasets – LRW [7], CelebA [35], FFHQ [25], MEAD [55], AffectNet [40], and BP4D [63] – covering in-the-wild photos/videos, high-quality portraits, controlled studio videos, and 4D expression scans. AffectNet uses the *AffectNet-7* protocol in our experiments, i.e., we discard *Contempt* and keep the six basic emotions plus *Nneutral* while retaining valence–arousal labels.

4.2. Evaluation

FIELDS is designed to improve in-the-wild facial expression recognition without sacrificing naturalness. Previous works [8, 18, 19] also show that geometric errors correlate poorly with perceived expressions because identity shape dominates geometric metrics. Therefore, we conduct three complementary evaluations: 1) Emotion Analysis, 2) Reconstruction fidelity via FLAME parameter loss, 3) Qualitative comparisons with side-by-side renderings.

Emotion Analysis. We evaluate how much affective information each 3D reconstruction preserves by following EMOCA [8]’s protocol: the predicted FLAME parameters of each method are used as 3D features to train a lightweight

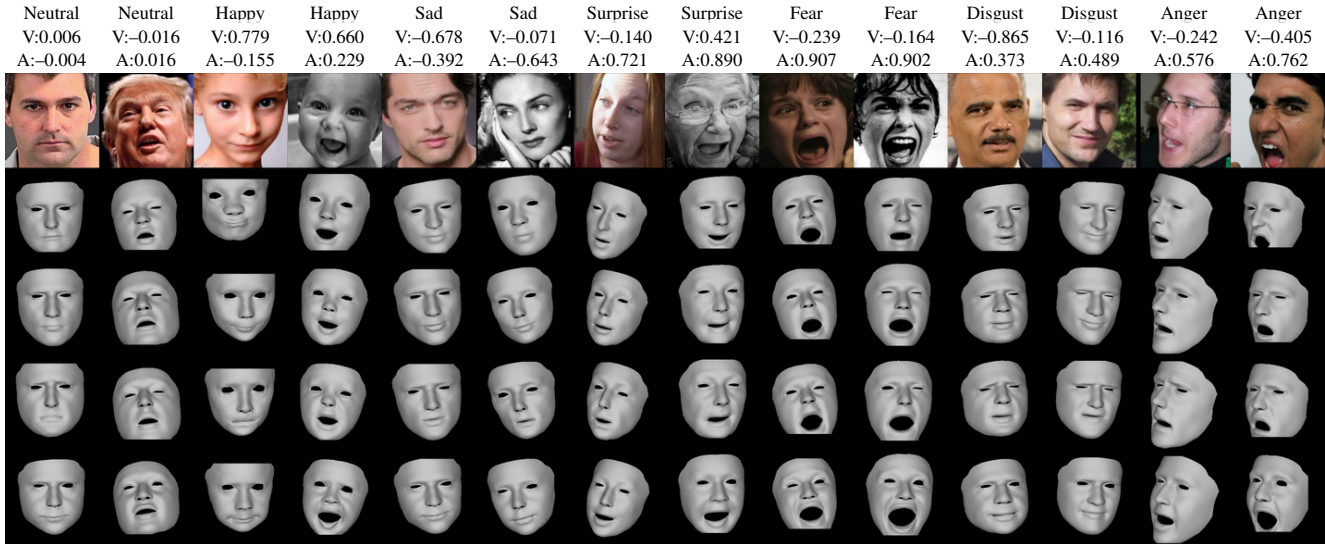


Figure 4. Visual Examples of 3D Face Reconstruction. From top to bottom: Emotion class label, Valence value label, Arousal value label, Input image, EMOCA [8], SMIRK [47], TEASER [34], FIELDS.

Table 1. Valence-arousal regression (5-fold). PCC/CCC/SAGR (means with superscripted std (\pm); higher is better). RMSE is lower-better. Best per column in **bold**.

Model	Valence (V)				Arousal (A)			
	V-PCC \uparrow	V-CCC \uparrow	V-RMSE \downarrow	V-SAGR \uparrow	A-PCC \uparrow	A-CCC \uparrow	A-RMSE \downarrow	A-SAGR \uparrow
EMOCA [8]	0.733 \pm 0.008	0.721 \pm 0.007	0.343 \pm 0.008	0.790 \pm 0.005	0.591 \pm 0.014	0.580 \pm 0.014	0.361 \pm 0.008	0.763 \pm 0.005
SMIRK [47]	0.702 \pm 0.004	0.690 \pm 0.001	0.363 \pm 0.005	0.781 \pm 0.005	0.551 \pm 0.004	0.538 \pm 0.004	0.376 \pm 0.003	0.745 \pm 0.004
TEASER [34]	0.724 \pm 0.005	0.715 \pm 0.005	0.348 \pm 0.004	0.787 \pm 0.003	0.583 \pm 0.006	0.573 \pm 0.009	0.366 \pm 0.006	0.757 \pm 0.009
FIELDS	0.747\pm0.003	0.737\pm0.006	0.338\pm0.006	0.801\pm0.002	0.616\pm0.008	0.604\pm0.008	0.352\pm0.011	0.764\pm0.008

Table 2. Emotion classification (5-fold). Means with superscripted std (\pm), shown as percentages. Best per column in **bold**.

Model	Accuracy($\%$) \uparrow	Precision($\%$) \uparrow	F1($\%$) \uparrow
EMOCA [8]	53.0 \pm 0.62	57.0 \pm 0.31	52.5 \pm 0.65
SMIRK [47]	48.7 \pm 0.62	53.5 \pm 0.46	48.0 \pm 0.91
TEASER [34]	55.3 \pm 0.51	57.7 \pm 0.67	55.1 \pm 0.71
FIELDS	56.0\pm1.5	59.3\pm0.59	55.6\pm1.6

4-layer MLP (BatchNormalization + LeakyReLU) for (i) discrete emotion classification and (ii) valence-arousal (VA) regression on AffectNet. Since the official AffectNet test set is no longer public, we perform 5-fold cross-validation on the official training split and report mean \pm std on the fold-specific, class-balanced validation sets to ensure fairness.

For **emotion classification**, we report Accuracy, Precision and F1 as shown in Tab. 2. For **valence-arousal**

regression, we report the Pearson Correlation Coefficient (PCC \uparrow), the Concordance Correlation Coefficient (CCC \uparrow), the Root Mean Squared Error (RMSE \downarrow), and Sign Agreement (SAGR \uparrow), each computed separately for valence and arousal in Tab. 1. FIELDS consistently outperforms prior reconstructions across all reported metrics, achieving the best results on AffectNet classification and on VA regression metrics. We additionally include **per-class results** as bar chart and **t-SNE/UMAP visualizations** of the learned 3D expression representations:

- **Per-class Accuracy.** From the grouped bars in Fig. 5, our method shows the clearest gains on *Happy/Neutral* and consistently strong results on *Fear*, matching our intensity-aware calibration. Classes that rely on fine wrinkles or intra-oral cues (*Disgust/Anger*) remain challenging due to 3DMM’s limited support for such details and the class imbalance in AffectNet.
- **t-SNE Clustering Visualization.** Fig. 6 shows t-SNE projections of FIELDS’ expression features. We observe compact within-class clusters separated by low-density

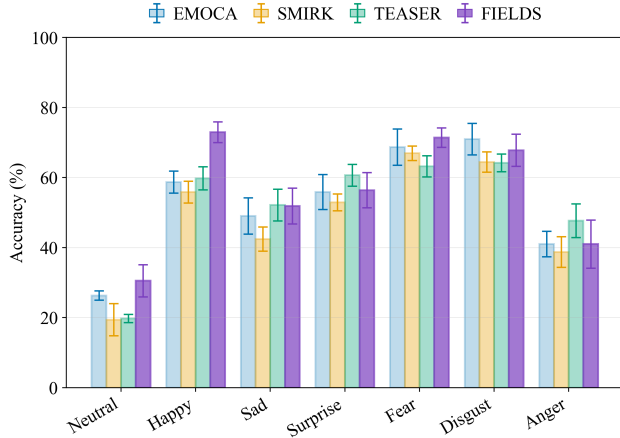


Figure 5. Emotion classification, per-class accuracy (mean±std) – grouped bars for each emotion.

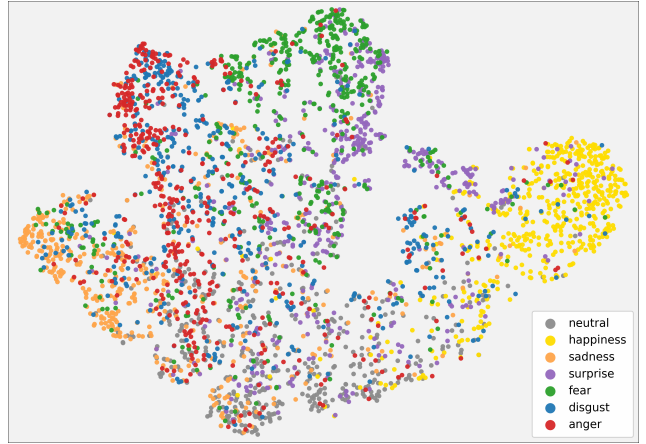
Table 3. FLAME parameter MSE on BP4D test subjects (lower is better). Best in **bold**.

FLAME Param	EMOCA [8]	SMIRK [47]	TEASER [34]	FIELDS
$\{\psi_{exp}, \theta_{jaw}\}$	1.273	1.277	3.345	0.173
β	–	0.426	0.431	0.349

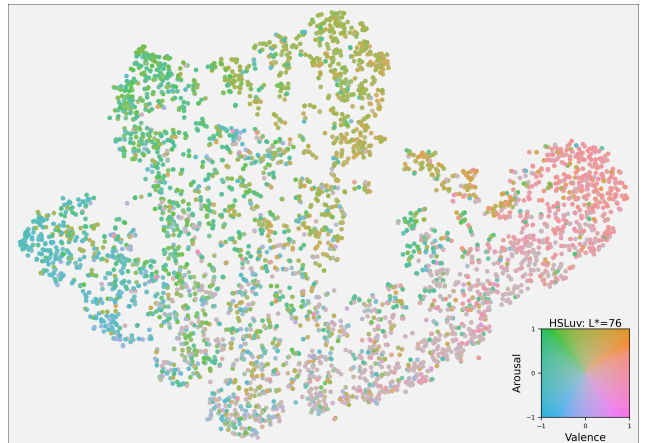
boundaries (e.g., *Happiness*, *Sadness*), with residual mixing mainly on known hard pairs (e.g., *Anger/Digust*). When colored by valence–arousal, the manifold exhibits a smooth VA gradient around the circumplex, indicating continuous affect encoding; intensity increases map to higher saturation. Cross-method comparisons are provided in the supplementary.

Reconstruction Fidelity. As repeatedly observed [8, 18, 19, 47], mesh/landmark geometric errors correlate poorly with perceived expressions and are largely driven by identity shape. Instead, we assess reconstruction fidelity by comparing each method’s predicted FLAME expression–jaw parameters to reference parameters obtained from a unified FLAME fitting on BP4D, reporting parameter-space MSE. Because FLAME decodes (locally) linearly from (ψ, θ_{jaw}) , smaller residuals imply less exaggerated, more faithful expressions. Evaluation uses a stratified BP4D split; procedural details are provided in the supplementary. For downstream stability we also report identity β -MSE; since EMOCA uses 100-D shape while others use 300-D, we omit cross-method β comparisons for EMOCA to keep fairness (Tab. 3).

Qualitative Comparisons. Fig. 4 shows side-by-side 3D mesh reconstructions on the AffectNet val set together with the corresponding emotion/VA labels. Across varied poses and intensities, our renderings convey the intended affect while avoiding common artifacts (e.g., excessive mouth opening, eyebrow overshoot, cheek inflation). Fine cues



(a) FIELDS – t-SNE colored according to emotion class



(b) FIELDS – t-SNE colored according to valence and arousal value

Figure 6. t-SNE visualization of FIELDS expression embeddings of the AffectNet val set. Each point is a projected expression feature; (Top) class coloring, color encodes the discrete emotion class; (Bottom) valence–arousal coloring (HSLuv, $L^*=76$), color encodes continuous valence–arousal value.

such as asymmetric smiles and slight frowns are retained, and the overall geometry remains natural and stable.

In Fig. 7 we present qualitative comparisons on BP4D: for each sample we show the input RGB image, the synchronized 3D scan, the fitted FLAME reference, and reconstructed mesh renderings side by side to evaluate expression fidelity. Our meshes closely follow the scan geometry: jaw opening and lip–corner displacement are calibrated, eyebrow elevation matches the reference without overshoot.

4.3. Ablation Study

Effect of Supervision. We ablate the two supervision signals – 3D parameter supervision \mathcal{L}_{3D-GT} and the intensity-aware emotion loss \mathcal{L}_{emo} – on a 2D-consistency baseline (Tab. 4). Adding \mathcal{L}_{3D-GT} chiefly *calibrates expression magnitude*, reducing BP4D parameter error

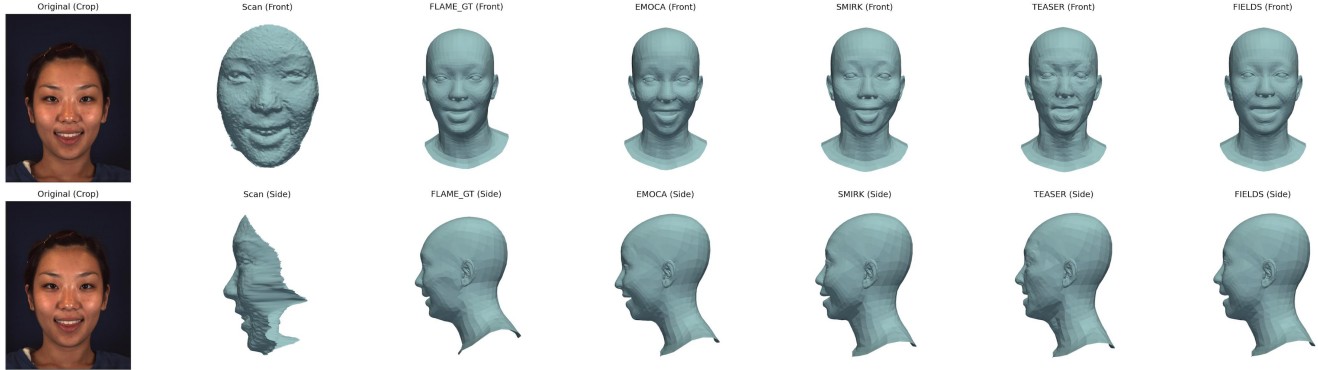


Figure 7. Visual examples of 3D face model and reconstruction in BP4D dataset, from left to right: BP4D original image, 3D scan, fitted FLAME model, EMOCA[8], SMIRK[47], TEASER[34], FIELDS.

Table 4. Unified ablation. Classification (over 5 folds) is reported as mean \pm std in percentages. VA regression (over 5 folds) reports mean \pm std for CCC/RMSE (\uparrow higher is better; \downarrow lower is better). FLAME parameter MSE (\downarrow lower is better). Best per column in **bold**.

Model	Emotion Classification (%)			V/A Regression				FLAME Param MSE (\downarrow)	
	Acc \uparrow	Prec \uparrow	F1 \uparrow	V-CCC \uparrow	V-RMSE \downarrow	A-CCC \uparrow	A-RMSE \downarrow	$\{\psi_{exp}, \theta_{jaw}\}$	β
F0: Pre-train	47.7 \pm 0.75	51.0 \pm 0.72	46.6 \pm 1.0	0.647 \pm 0.008	0.384 \pm 0.005	0.528 \pm 0.012	0.378 \pm 0.009	0.678	0.357
F1: Baseline	52.3 \pm 0.67	55.1 \pm 0.25	51.6 \pm 0.92	0.686 \pm 0.011	0.367 \pm 0.006	0.560 \pm 0.009	0.366 \pm 0.004	5.954	0.354
F2: F1+ \mathcal{L}_{3D-GT}	51.8 \pm 0.67	55.6 \pm 0.56	51.1 \pm 0.74	0.705 \pm 0.010	0.353 \pm 0.006	0.568 \pm 0.006	0.367 \pm 0.005	0.159	0.354
F3: F1+ \mathcal{L}_{emo}	54.3 \pm 1.6	58.7 \pm 0.51	53.9 \pm 1.6	0.740\pm0.009	0.336\pm0.005	0.609\pm0.009	0.348\pm0.006	3.161	0.354
F4: F2+F3	56.0\pm1.5	59.3\pm0.59	55.6\pm1.6	0.737 \pm 0.006	0.338 \pm 0.006	0.604 \pm 0.008	0.352 \pm 0.011	0.173	0.349

and improving valence consistency, which indicates less over/under-shooting. Adding \mathcal{L}_{emo} primarily *injects affect semantics*, lifting VA correlation and improving emotion classification.

Together the results match the design: \mathcal{L}_{3D-GT} anchors the encoder in parameter space, shrinking BP4D expression-jaw MSE by an order of magnitude and improving V-CCC/RMSE. In contrast, \mathcal{L}_{emo} raises VA correlation (PCC/CCC) and AffectNet F1 simultaneously, evidencing that the learned codes carry *more affect semantics* rather than merely changing decision thresholds. Their combination preserves near-peak VA while delivering the best classification, showing the signals are complementary (magnitude control + semantic alignment) rather than redundant.

4.4. Discussion and analysis

Our experimental results indicate a controllable trade space between geometric fidelity and affect sensitivity. FIELDS is intentionally positioned toward *emotion readiness*: direct supervision on FLAME expression parameters reduces decoder compensation, while the intensity-aware emotion loss curbs over-amplification, yielding semantically calibrated expressions and consistent gains on FER/VA.

Purely geometric errors (*e.g.*, vertex MSE) are imperfect proxies for expression fidelity and subtle affect. Eval-

uating in the 3DMM’s disentangled expression space therefore reveals improvements that may be muted in mesh-level metrics. A remaining gap between the parameter space and the mesh/image space – stemming from basis conditioning, regularization, and rendering – can lead to different rankings across metrics, highlighting the complementarity of geometry- and affect-oriented objectives and the need for cross-space evaluation.

5. Conclusions

We present a 3DMM-centric framework for emotion-aware face reconstruction that unifies 2D consistency with two parameter-space signals: direct expression supervision and an intensity-aware emotion objective. The captured 3DMM features are more affect-aligned, improving both discrete FER and continuous VA regression while preserving high-fidelity face reconstruction. While the proposed paradigm focuses affect preservation and relies on per-frame processing, geometry-critical applications may prefer different trade-offs. Extending FIELDS by integrating temporal cues, adaptive loss weights $\lambda_{emo}/\lambda_{3D-GT}$, and Facial Action Unit priors is left for future work. We believe this hybrid supervision recipe can serve as a simple and reproducible baseline for FER-ready 3D facial representations.

Acknowledgements. This work was supported by the Wallenberg AI, Autonomous Systems and Software Program (WASP) funded by the Knut and Alice Wallenberg Foundation, and the Swedish e-Science Research Centre (SeRC). Some of the computations were enabled by the supercomputing resources Berzelius and LUMI provided by the National Supercomputer Centre at Linköping University and the Knut and Alice Wallenberg foundation.

References

- [1] Riza Alp Guler, George Trigeorgis, Epameinondas Antonakos, Patrick Snape, Stefanos Zafeiriou, and Iasonas Kokkinos. Densereg: Fully convolutional dense shape regression in-the-wild. In *IEEE/CVF Conference on Computer Vision and Pattern Recognition*, 2017. 3
- [2] Hela Bejaoui, Haythem Ghazouani, and Walid Barhoumi. Fully automated facial expression recognition using 3D morphable model and mesh-local binary pattern. In *International Conference on Advanced Concepts for Intelligent Vision Systems*, pages 39–50, 2017. 3
- [3] Volker Blanz and Thomas Vetter. A morphable model for the synthesis of 3D faces. In *ACM SIGGRAPH*, 1999. 1, 2
- [4] Volker Blanz, Sami Romdhani, and Thomas Vetter. Face identification across different poses and illuminations with a 3D morphable model. In *IEEE International Conference on Automatic Face & Gesture Recognition*, 2002. 3
- [5] Adrian Bulat and Georgios Tzimiropoulos. How far are we from solving the 2D & 3D face alignment problem? (and a dataset of 230,000 3D facial landmarks). In *IEEE International Conference on Computer Vision*, 2017. 1, 2
- [6] Feng-Ju Chang, Anh Tuan Tran, Tal Hassner, Iacopo Masi, Ram Nevatia, and Gerard Medioni. Expnet: Landmark-free, deep, 3D facial expressions. In *IEEE International Conference on Automatic Face & Gesture Recognition*, 2018. 3
- [7] Joon Son Chung and Andrew Zisserman. Lip reading in the wild. In *Asian Conference on Computer Vision*, 2017. 5, 1
- [8] Radek Daněček, Michael J Black, and Timo Bolkart. Emoca: Emotion driven monocular face capture and animation. In *IEEE/CVF Conference on Computer Vision and Pattern Recognition*, 2022. 2, 3, 5, 6, 7, 8
- [9] Yu Deng, Jiaolong Yang, Sicheng Xu, Dong Chen, Yunde Jia, and Xin Tong. Accurate 3D face reconstruction with weakly-supervised learning: From single image to image set. In *IEEE/CVF Conference on Computer Vision and Pattern Recognition Workshops*, 2019. 2
- [10] Yu Deng, Jiaolong Yang, Sicheng Xu, Dong Chen, Yunde Jia, and Xin Tong. Accurate 3D face reconstruction with weakly-supervised learning: From single image to image set. In *IEEE/CVF Conference on Computer Vision and Pattern Recognition Workshops*, 2019. 3
- [11] Haojie Diao, Xingguo Jiang, Yang Fan, Ming Li, and Hongcheng Wu. 3D face reconstruction based on a single image: a review. *IEEE Access*, 12:59450–59473, 2024. 3
- [12] Lu Dong, Xiao Wang, Srirangaraj Setlur, Venu Govindaraju, and Ifeoma Nwogu. IG3D: Integrating 3D face representations in facial expression inference. In *European Conference on Computer Vision*, 2025. 3
- [13] Bernhard Egger, William AP Smith, Ayush Tewari, Stefanie Wuhrer, Michael Zollhoefer, Thabo Beeler, Florian Bernard, Timo Bolkart, Adam Kortylewski, Sami Romdhani, et al. 3D morphable face models—past, present, and future. *ACM Transactions on Graphics*, 39(5):1–38, 2020. 1, 2
- [14] Paul Ekman. Universals and cultural differences in facial expressions of emotion. In *Nebraska Symposium on Motivation*, 1971. 1, 2
- [15] Lisa Feldman Barrett and James A Russell. Independence and bipolarity in the structure of current affect. *Journal of Personality and Social Psychology*, 74(4):967, 1998. 2
- [16] Yao Feng, Haiwen Feng, Michael J Black, and Timo Bolkart. Learning an animatable detailed 3D face model from in-the-wild images. *ACM Transactions on Graphics*, 40(4):1–13, 2021. 2, 3
- [17] Chiara Filippini, David Perpetuini, Daniela Cardone, and Arangelo Merla. Improving human–robot interaction by enhancing nao robot awareness of human facial expression. *Sensors*, 21(19):6438, 2021. 1
- [18] Panagiotis P Filntisis, George Retsinas, Foivos Paraperas-Papantoniou, Athanasios Katsamanis, Anastasios Roussos, and Petros Maragos. Spectre: Visual speech-informed perceptual 3D facial expression reconstruction from videos. In *IEEE/CVF Conference on Computer Vision and Pattern Recognition*, 2023. 5, 7
- [19] Pablo Garrido, Michael Zollhöfer, Chenglei Wu, Derek Bradley, Patrick Pérez, Thabo Beeler, and Christian Theobalt. Corrective 3D reconstruction of lips from monocular video. *ACM Transactions on Graphics*, 35(6):219–1, 2016. 5, 7
- [20] Kyle Genova, Forrester Cole, Aaron Maschinot, Aaron Sarna, Daniel Vlasic, and William T. Freeman. Unsupervised training for 3D morphable model regression. In *IEEE Conference on Computer Vision and Pattern Recognition*, 2018. 3
- [21] Thomas Gerig, Andreas Morel-Forster, Clemens Blumer, Bernhard Egger, Marcel Luthi, Sandro Schönborn, and Thomas Vetter. Morphable face models—an open framework. In *IEEE International Conference on Automatic Face & Gesture Recognition*, 2018. 3
- [22] Jia Guo and Jiankang Deng. InsightFace: 2D and 3D face analysis project. <https://github.com/deepinsight/insightface>, 2022. 1
- [23] Jianzhu Guo, Xiangyu Zhu, Yang Yang, Fan Yang, Zhen Lei, and Stan Z Li. Towards fast, accurate and stable 3D dense face alignment. In *European Conference on Computer Vision*, 2020. 3
- [24] Mohan Karnati, Ayan Seal, Debotosh Bhattacharjee, Anis Yazidi, and Ondrej Krejcar. Understanding deep learning techniques for recognition of human emotions using facial expressions: A comprehensive survey. *IEEE Transactions on Instrumentation and Measurement*, 72:1–31, 2023. 1, 2
- [25] Tero Karras, Samuli Laine, and Timo Aila. A style-based generator architecture for generative adversarial networks. In *IEEE/CVF Conference on Computer Vision and Pattern Recognition*, 2019. 5, 1
- [26] Haider A Kassem, Morshed Chowdhury, and Jemal H Abawajy. Drivers fatigue level prediction using facial, and

- head behavior information. *IEEE Access*, 9:121686–121697, 2021. 1
- [27] Tatsuro Koizumi and William AP Smith. “Look Ma, no landmarks!” – unsupervised, model-based dense face alignment. In *European Conference on Computer Vision*, 2020. 3
- [28] Mohammad Rami Koujan, Luma Alharbawee, Giorgos Giannakakis, Nicolas Pugeault, and Anastasios Roussos. Real-time facial expression recognition “in the wild” by disentangling 3D expression from identity. In *IEEE International Conference on Automatic Face & Gesture Recognition*, 2020. 3
- [29] Eva G Krumhuber, Lina I Skora, Harold CH Hill, and Karen Landier. The role of facial movements in emotion recognition. *Nature Reviews Psychology*, 2(5):283–296, 2023. 1
- [30] Shan Li and Weihong Deng. Deep facial expression recognition: A survey. *IEEE Transactions on Affective Computing*, 13(3):1195–1215, 2020. 1, 2
- [31] Tianye Li, Timo Bolkart, Michael J Black, Hao Li, and Javier Romero. Learning a model of facial shape and expression from 4D scans. *ACM Transactions on Graphics*, 36(6):194–1, 2017. 1, 2, 3
- [32] Tianye Li, Timo Bolkart, Michael J. Black, Hao Li, and Javier Romero. TF-FLAME. https://github.com/TimoBolkart/TF_FLAME, 2021. 4
- [33] Yaojie Liu, Amin Jourabloo, William Ren, and Xiaoming Liu. Dense face alignment. In *IEEE International Conference on Computer Vision Workshops*, 2017. 3
- [34] Yunfei Liu, Lei Zhu, Lijian Lin, Ye Zhu, Ailing Zhang, and Yu Li. Teaser: Token enhanced spatial modeling for expressions reconstruction. In *International Conference on Learning Representations*, 2025. 2, 3, 4, 5, 6, 7, 8, 1
- [35] Ziwei Liu, Ping Luo, Xiaogang Wang, and Xiaoou Tang. Deep learning face attributes in the wild. In *IEEE International Conference on Computer Vision*, 2015. 5, 1
- [36] Camillo Lugaresi, Jiuqiang Tang, Hadon Nash, Chris McClanahan, Esha Ubowaja, Michael Hays, Fan Zhang, Chuoling Chang, Ming Guang Yong, Juhyun Lee, et al. Mediapipe: A framework for building perception pipelines. *arXiv preprint arXiv:1906.08172*, 2019. 1, 2
- [37] Chenlei Lv, Zhongke Wu, Xingce Wang, and Mingquan Zhou. 3D facial expression modeling based on facial landmarks in single image. *Neurocomputing*, 355:155–167, 2019. 2
- [38] Kenji Mase. Recognition of facial expression from optical flow. *IEICE Transactions on Information and Systems*, 74(10):3474–3483, 1991. 2
- [39] Albert Mehrabian. *Silent Messages*. Wadsworth, Belmont, CA, 1st edition, 1971. 1
- [40] Ali Mollahosseini, Behzad Hasani, and Mohammad H Mahoor. AffectNet: A database for facial expression, valence, and arousal computing in the wild. *IEEE Transactions on Affective Computing*, 10(1):18–31, 2017. 5, 1
- [41] Duc-Phong Nguyen, Marie-Christine Ho Ba Tho, and Tien-Tuan Dao. Enhanced facial expression recognition using 3D point sets and geometric deep learning. *Medical & Biological Engineering & Computing*, 59(6):1235–1244, 2021. 2
- [42] Omar Ocegueda, Tianhong Fang, Shishir K. Shah, and Ioannis A. Kakadiaris. Expressive maps for 3D facial expression recognition. In *IEEE International Conference on Computer Vision Workshops*, 2011. 2
- [43] Pascal Paysan, Reinhard Knothe, Brian Amberg, Sami Romdhani, and Thomas Vetter. A 3D face model for pose and illumination invariant face recognition. In *IEEE International Conference on Advanced Video and Signal Based Surveillance*, 2009. 2
- [44] Ercheng Pei, Meshia Cedric Oveneke, Yong Zhao, Dongmei Jiang, and Hichem Sahli. Monocular 3D facial expression features for continuous affect recognition. *IEEE Transactions on Multimedia*, 23:3540–3550, 2020. 3
- [45] Melpo Pittara, Andreas Anastasiou, Konstantinos Andreou, Andreas Panayides, Nicolai Petkov, and Constantinos S. Pattichis. Facial image and video pain intensity estimation. In *Asilomar Conference on Signals, Systems, and Computers*, 2024. 1
- [46] Stylianos Ploumpis, Evangelos Ververas, Eimear O’Sullivan, Stylianos Moschoglou, Haoyang Wang, Nick Pears, William AP Smith, Baris Gecer, and Stefanos Zafeiriou. Towards a complete 3D morphable model of the human head. *IEEE Transactions on Pattern Analysis and Machine Intelligence*, 43(11):4142–4160, 2020. 3
- [47] George Retsinas, Panagiotis P. Filntisis, Radek Daněček, Victoria F. Abrevaya, Anastasios Roussos, Timo Bolkarr, and Petros Maragos. 3D facial expressions through analysis-by-neural-synthesis. In *IEEE/CVF Conference on Computer Vision and Pattern Recognition*, 2024. 2, 3, 5, 6, 7, 8, 1
- [48] James A Russell. A circumplex model of affect. *Journal of personality and social psychology*, 39(6):1161, 1980. 2
- [49] Soubhik Sanyal, Timo Bolkart, Haiwen Feng, and Michael J Black. Learning to regress 3D face shape and expression from an image without 3D supervision. In *IEEE/CVF Conference on Computer Vision and Pattern Recognition*, 2019. 2
- [50] Jiayang Shang, Tianwei Shen, Shiwei Li, Lei Zhou, Mingmin Zhen, Tian Fang, and Long Quan. Self-supervised monocular 3D face reconstruction by occlusion-aware multi-view geometry consistency. In *European Conference on Computer Vision*, 2020. 3
- [51] Sahil Sharma and Vijay Kumar. 3D face reconstruction in deep learning era: A survey. *Archives of Computational Methods in Engineering*, 29(5):3475–3507, 2022. 1, 3
- [52] Mani Kumar Tellamekala, Ömer Sümer, Björn W Schuller, Elisabeth André, Timo Giesbrecht, and Michel Valstar. Are 3D face shapes expressive enough for recognising continuous emotions and action unit intensities? *IEEE Transactions on Affective Computing*, 2023. 3
- [53] Ayush Tewari, Michael Zollhofer, Hyeonwoo Kim, Pablo Garrido, Florian Bernard, Patrick Perez, and Christian Theobalt. MOFA: Model-based deep convolutional face autoencoder for unsupervised monocular reconstruction. In *IEEE International Conference on Computer Vision Workshops*, 2017. 1
- [54] Anh Tuan Tran, Tal Hassner, Iacopo Masi, and Gérard Medioni. Regressing robust and discriminative 3D morphable models with a very deep neural network. In

- IEEE/CVF Conference on Computer Vision and Pattern Recognition*, 2017. 3
- [55] Kaisiyuan Wang, Qianyi Wu, Linsen Song, Zhuoqian Yang, Wayne Wu, Chen Qian, Ran He, Yu Qiao, and Chen Change Loy. Mead: A large-scale audio-visual dataset for emotional talking-face generation. In *European Conference on Computer Vision*, 2020. 5, 1
- [56] Yan Wang, Shaoqi Yan, Yang Liu, Wei Song, Jing Liu, Yang Chang, Xinji Mai, Xiping Hu, Wenqiang Zhang, and Zhongxue Gan. A survey on facial expression recognition of static and dynamic emotions. *arXiv preprint arXiv:2408.15777*, 2024. 1, 2
- [57] Sherri C Widen and James A Russell. Children acquire emotion categories gradually. *Cognitive development*, 23(2): 291–312, 2008. 2
- [58] JC Wojdel, A Wojdel, and LJM Rothkrantz. Analysis of facial expressions based on silhouettes. In *Fifth Annual Conference of ASCI*, 1999. 2
- [59] E Wood, T Baltrusaitis, C Hewitt, M Johnson, J Shen, N Milosavljevic, D Wilde, S Garbin, T Sharp, I Stojiljkovic, et al. 3D face reconstruction with dense landmarks. *arXiv preprint arXiv:2204.02776*, 2022. 3
- [60] Fanzi Wu, Linchao Bao, Yajing Chen, Yonggen Ling, Yibing Song, Songnan Li, King Ngi Ngan, and Wei Liu. MVF-Net: Multi-view 3D face morphable model regression. In *IEEE/CVF Conference on Computer Vision and Pattern Recognition*, 2019. 3
- [61] Haotian Yang, Hao Zhu, Yanru Wang, Mingkai Huang, Qiu Shen, Ruigang Yang, and Xun Cao. Facescape: a large-scale high quality 3D face dataset and detailed riggable 3D face prediction. In *IEEE/CVF Conference on Computer Vision and Pattern Recognition*, 2020. 3
- [62] Richard Zhang, Phillip Isola, Alexei A Efros, Eli Shechtman, and Oliver Wang. The unreasonable effectiveness of deep features as a perceptual metric. In *IEEE/CVF Conference on Computer Vision and Pattern Recognition*, 2018. 3
- [63] Xing Zhang, Lijun Yin, Jeffrey F Cohn, Shaun Canavan, Michael Reale, Andy Horowitz, Peng Liu, and Jeffrey M Girard. BP4D-Spontaneous: a high-resolution spontaneous 3D dynamic facial expression database. *Image and Vision Computing*, 32(10):692–706, 2014. 2, 3, 4, 5, 1
- [64] Sicheng Zhao, Xiaopeng Hong, Jufeng Yang, Yanyan Zhao, and Guiguang Ding. Toward label-efficient emotion and sentiment analysis. *Proceedings of the IEEE*, 111(10):1159–1197, 2023. 1
- [65] Xi Zhao, Jianhua Zou, Huibin Li, Emmanuel Dellandréa, Ioannis A. Kakadiaris, and Liming Chen. Automatic 2.5-D facial landmarking and emotion annotation for social interaction assistance. *IEEE Transactions on Cybernetics*, 46(9): 2042–2055, 2016. 2
- [66] Kangkang Zhu, Yunhong Wang, Hongyu Yang, Di Huang, and Liming Chen. Intensity enhancement via GAN for multimodal facial expression recognition. In *IEEE International Conference on Image Processing*, 2020. 2
- [67] Wojciech Zielonka, Timo Bolkart, and Justus Thies. Towards metrical reconstruction of human faces. In *European Conference on Computer Vision*, 2022. 3, 5, 2

FIELDS: Face reconstruction with accurate Inference of Expression using Learning with Direct Supervision

Supplementary Material

6. Implementation Details

Datasets. The proposed method is trained and evaluated on six publicly available benchmark datasets: LRW [7], CelebA [35], FFHQ [25], MEAD [55], AffectNet [40], and BP4D [63]. **LRW** contains over 500,000 short video clips (each video has 29 frames, totaling 1.6 seconds) of 500 target words spoken by hundreds of different speakers. **CelebA** comprises 202,599 face images of 10 177 identities under diverse poses, expressions, and backgrounds. **FFHQ** offers 70,000 high-quality, 1024×1024 resolution face images sampled from Flickr albums. It covers a wide range of ages, ethnicities, and backgrounds. **MEAD** provides over 42 000 video clips of 60 actors uttering scripted sentences under six basic emotions in the lab environment. **BP4D** is a 4D facial expression dataset with synchronized high-resolution RGB video and 3D dynamic scans from 41 participants performing ten emotion-elicitation tasks. **AffectNet** is drawn from ‘in the wild’ photos sourced from the Web. This subset of 291,651 facial images was manually annotated with one of eight discrete emotion categories (labels 0–7) as well as Valence/Arousal values.

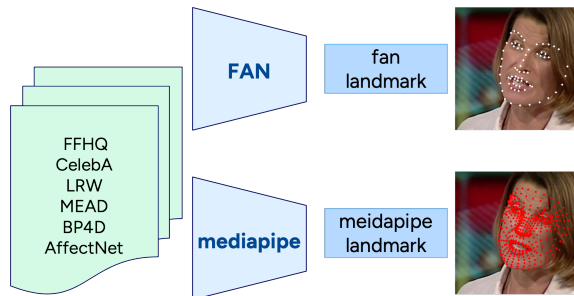


Figure 8. Data Pre-Processing Pipeline.

Data Pre-processing Details. All datasets undergo facial landmark detection using MediaPipe [36] and FAN [5]. The Insight Face 203 landmarks [22] which is applied in TEASER [34] are detected during training. Based on the MediaPipe landmarks, we crop each face to a 224×224 resolution (Fig. 8). For video datasets, we randomly sample frames from each clip. Following SMIRK [47], we use mixed-dataset, frames from different datasets are drawn according to a predefined sampling ratio during training and validation.

Pre-training Details. As illustrated in Fig. 9, the goal of pre-training stage is to obtain a stable encoder for FLAME parameters (shape β , expression Ψ , pose Θ) *without* using

the synthesizer, by anchoring identity to MICA and aligning geometry with 2D landmarks.

We optimize only the parameter encoder with a landmark reprojection term and a MICA shape term:

$$\mathcal{L}_{\text{pre}} = \lambda_{\text{lmk}} \left(\|\hat{K} - K^{\text{mp}}\|_2^2 + \|\hat{K} - K^{\text{fan}}\|_2^2 \right) + \lambda_{\text{mica}} \|\hat{\beta} - \beta_{\text{mica}}\|_2^2, \quad (12)$$

where \hat{K} are projected 3D landmarks from the FLAME given $(\hat{\beta}, \hat{\Phi}, \hat{\Theta})$; we obtain 2D landmarks $\{K^{\text{mp}}, K^{\text{fan}}\}$ from data pre-processing; the loss weights $\lambda_{\text{lmk}} = 100$ and $\lambda_{\text{mica}} = 10$. No renderer/token branch or pixel/perceptual losses are used in this stage.

Only the FLAME-parameter encoder is updated; the synthesizer and token encoder are not used. Model selection/early stopping is based on the validation of MICA shape loss. The resulting encoder is taken as the *base model B* for the main training and for later regularization.

Training Setting. For the encoder objective in Eq. (10), we set overall loss weights $\lambda_{2D} = 1$ and the corresponding loss weights vector in Eq. (8) as $\mathbf{w}_{2D} = (10, 10, 10, 100, 500)$. The emotion term uses $\lambda_{\text{emo}} = 5$ with $\lambda_r = 1$ and $\lambda_c = 1$ in Eq. (7); the parameter regularizer in Eq. (9) uses $\lambda_{\text{shape-reg}} = 100$ and $\lambda_{\text{expr-reg}} = 10^{-2}$. For the synthesizer objective in Eq. (11), we reuse the same $\mathcal{L}_{2D\text{-cons}}$ weights, and set $\lambda_{\text{exp}} = \lambda_{\text{token}} = 1$. We train for at most 90 epochs with Adam ($\text{lr} = 2 \times 10^{-3}$) and batch size 64. A two-stage schedule is used: epochs 1–6 sample BP4D at 30% with the weight $\lambda_{3D} = 5$; epochs 7–90 use BP4D at 10% with $\lambda_{3D} = 1$. The cross-dataset sampling ratios are LRW 20%, CelebA 26%, AffectNet 26%, FFHQ 10%, and MEAD 8%.

7. BP4D FLAME Fitting and Data Split

We fit each frame of the BP4D dataset to the FLAME head model to obtain compatible pose, shape, and expression parameters, as well as mesh models as ground truth that will be used for model training and evaluation.

Scan Pre-processing. BP4D scans contain hair regions and various noisy surface points, while the FLAME model does not include vertices corresponding to hair. To ensure accurate registration, we first remove these undesired regions from the raw scans. We use the ground-truth 83 3D facial landmarks as a reference to determine which regions should be retained. Specifically, we construct an ellipse that tightly encloses all 83 landmarks after projecting them onto a common plane. We first estimate the best-fitting plane for the

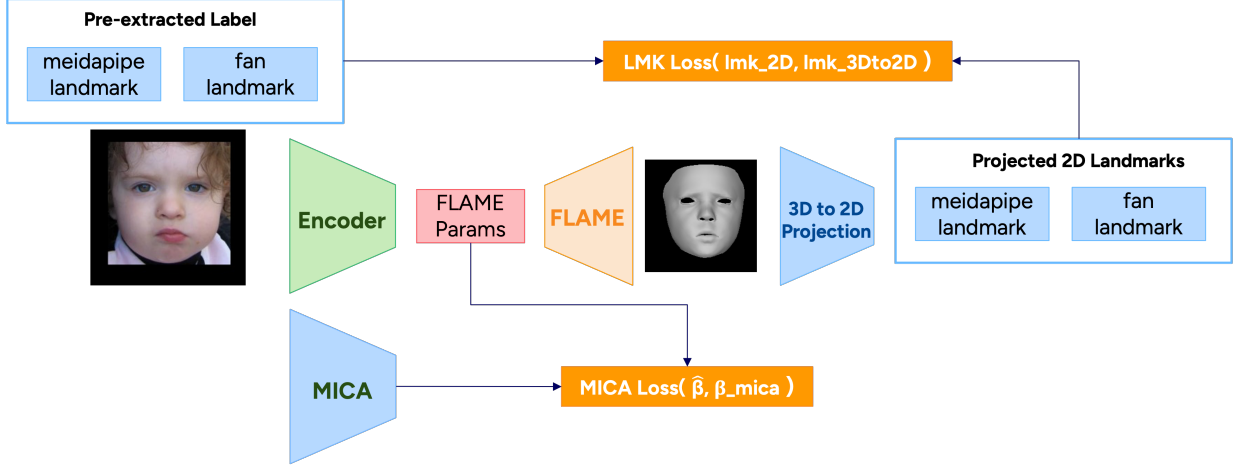


Figure 9. Illustration of the pre-training pipeline. Given an input image, the reconstruction encoder predicts FLAME parameters $(\hat{\beta}, \hat{\Phi}, \hat{\Theta})$. FLAME maps these parameters to a mesh and 3D landmarks, which are differentially projected to image space. In parallel, two sets of 2D landmarks are pre-extracted by MediaPipe [36] and FAN [5] as shown details in Fig. 8. MICA [67] is run on I to obtain a reference identity shape β_{mica} .

83 landmarks using principal component analysis (PCA). The plane is defined by the first two principal components, which correspond to the directions of maximum variance among the landmarks. We then project all 83 landmarks into this 2D plane and compute the radii of the ellipse:

$$r_a = \max(|u|), \quad r_b = \max(|v|),$$

where (u, v) are the 2D coordinates of the projected landmarks along the two principal axes. The elliptical region is therefore defined as:

$$\left(\frac{u}{r_a}\right)^2 + \left(\frac{v}{r_b}\right)^2 \leq 1 \quad (13)$$

Finally, we project all scan points onto the same PCA plane and retain those whose projected coordinates satisfy the elliptical constraint. This effectively removes hair and outlier regions while preserving the facial surface. An example of the raw scan (gray), the landmarks with the fitted ellipse (red), and the resulting preprocessed scan (blue) is shown in Fig. 10.

Fit FLAME to a 3D Scan. We employ the official FLAME fitting procedure [31], which optimizes the model parameters by jointly minimizing the scan-to-mesh distance, the 3D landmark alignment error, and several regularization terms on shape, pose, and expression. The weights for the scan distance, landmark, shape, pose, and expression term are set to 2.0, 0.1, $1e-4$, $1e-3$, and $1e-4$, respectively.

Data Split. We use a subject-exclusive, stratified split over the six strata $\{\text{Asian, White, Black}\} \times \{\text{Male, Female}\}$. From the 41 subjects, we allocate 6 to *val* and 6 to *test* – one subject per stratum in each split (uniform $1/6$ per stratum) – and use the remaining 29 for *train*. This yields the following

per-split composition (proportions computed over subjects in the split):

- **Train** (29 subjects; 269,161 samples): White_M 0.414, White_F 0.241, Asian_F 0.207, Black_F 0.138 (*no* Asian_M / Black_M in train due to subject count).
- **Val** (6 subjects; 50,455 frames): *F014* (Asian, F), *F019* (White, F), *F023* (Black, F), *M003* (Black, M), *M008* (Asian, M), *M009* (White, M).
- **Test** (6 subjects; 47,734 frames): *F010* (White, F), *F011* (Black, F), *F021* (Asian, F), *M004* (White, M), *M005* (Asian, M), *M017* (Black, M).

Dataset sizes (images/frames): *train* 269,161, *val* 50,455, *test* 47,734. This subject-level stratification prevents identity leakage while ensuring that both *val* and *test* cover all race-gender strata uniformly.

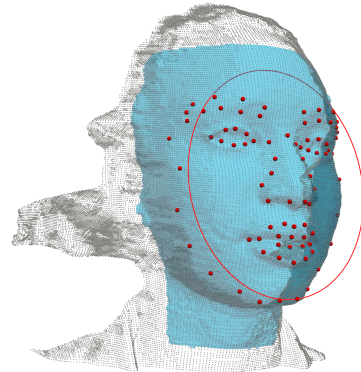


Figure 10. An example of the raw scan (gray), the landmarks with the fitted ellipse (red), and the resulting preprocessed scan (blue).

Table 5. Unified ablation on emotion loss weight. Classification (over 5 folds) is reported as mean \pm std in percentages. VA regression (over 5 folds) reports mean \pm std for CCC/RMSE (\uparrow higher is better; \downarrow lower is better). FLAME parameter MSE (\downarrow lower is better). Best per column in **bold**.

Model	Emotion Classification (%)			V/A Regression				FLAME Param MSE (\downarrow)	
	Acc \uparrow	Prec \uparrow	F1 \uparrow	V-CCC \uparrow	V-RMSE \downarrow	A-CCC \uparrow	A-RMSE \downarrow	$\{\psi_{exp}, \theta_{jaw}\}$	β
$\lambda_{emo} = 0.5$	54.3 \pm 1.8	57.8 \pm 0.92	54.0 \pm 1.8	0.719 \pm 0.005	0.346 \pm 0.006	0.592 \pm 0.007	0.354 \pm 0.008	0.188	0.355
$\lambda_{emo} = 1$	54.2 \pm 1.2	58.2 \pm 0.49	53.6 \pm 1.2	0.726 \pm 0.006	0.344 \pm 0.005	0.588 \pm 0.012	0.355 \pm 0.004	0.176	0.357
$\lambda_{emo} = 5(\text{Ours})$	56.0\pm1.5	59.3 \pm 0.59	55.6\pm1.6	0.737\pm0.006	0.338\pm0.006	0.604 \pm 0.008	0.352 \pm 0.011	0.173	0.349
$\lambda_{emo} = 10$	55.7 \pm 1.4	59.9\pm0.40	55.2 \pm 1.6	0.735 \pm 0.003	0.340 \pm 0.003	0.613\pm0.004	0.345\pm0.005	0.195	0.353

8. Additional Experiments

8.1. 3D Reconstruction Performance

Quantitative Evaluation. We assess reconstruction with three 3D metrics. **Keypoint Error:** the mean Euclidean distance (mm; lower is better) between 49 FLAME keypoints (barycentric on the predicted mesh) and BP4D references—captures expression amplitude at salient sites; **Vertex Error:** the mean Euclidean distance (mm; lower is better) over all mesh vertices between the predicted FLAME mesh and the fitted reference—measures dense surface fidelity; For distributional robustness, we report the area under the cumulative error distribution (CED) curve (AUC) of 3D distances. **AUC@0.1/5.0** denotes the area under the CED over [0, 0.1] mm and [0, 5] mm (higher is better).

We extract FLAME parameters on the BP4D test split from each reconstruction method, generate the corresponding meshes, and compare them against our FLAME-fitted BP4D references. As shown in Tab. 6, FIELDS is geometrically close to the best: its vertex error (0.0998 \pm 0.0292 mm) is essentially tied with TEASER/SMIRK (0.0989 mm), and AUC@5.0 is identical (0.982). Keypoint error is slightly higher than TEASER but comparable, while FIELDS clearly surpasses EMOCA on both keypoints and vertices – showing that adding affect supervision does not hurt geometry. At a strict tolerance (0.1 mm) the small gap reflects very fine, high-frequency details; at 5 mm all methods saturate. Crucially, FIELDS achieves the best AffectNet classification and VA regression (Tabs. 1 and 2). In summary, FIELDS is on par with geometry-centric SOTA and markedly better than EMOCA in geometry, while achieving the strongest emotion classification and VA regression; in other words, it attains stronger affect separability and calibrated expression magnitude at minimal geometric cost, aligning with the goal of emotion-aware reconstruction.

Qualitative Comparison. We show the 3D face mesh comparison on BP4D test split set according to gender in Fig. 12 and Fig. 13; FIELDS adheres more closely to the scan/FLAME reference and avoids common exaggeration artifacts (*e.g.*, over-opened mouth and eyebrow overshoot).

Table 6. Geometric performance on BP4D test set. 3D errors are reported as mean \pm std, lower is better; CED AUC is shown with 3 decimals, higher is better; Best per column in **bold**.

Model	3D errors (mm) \downarrow		CED AUC \uparrow	
	Keypoints	Vertices	AUC@0.1	AUC@5.0
EMOCA[8]	108 \pm 31	0.1111 \pm 0.0321	0.001	0.979
SMIRK[47]	97.5 \pm 29	0.0989\pm0.0297	0.446	0.982
TEASER[34]	96.3\pm29	0.0989\pm0.0291	0.463	0.982
FIELDS	97.7 \pm 29	0.0998 \pm 0.0292	0.444	0.982

8.2. Ablation on Supervision

Effect of Supervision Signals We conduct an ablation of the supervision signals on the BP4D test set, assessed via 3D reconstruction metrics. From Tab. 7, the 2D-only baseline (F1) attains the strongest strict geometric accuracy (best keypoint/vertex error and AUC@0.1), showing the efficacy of 2D consistency for pure geometry. Adding direct 3D supervision (F2) preserves geometry while better calibrating expression magnitude. Adding the intensity-aware emotion loss (F3) keeps overall robustness (AUC@5.0 unchanged) with a slight drop at very tight thresholds—consistent with suppressing over-exaggerated, high-frequency deformations. Combining both signals (F4) recovers much of the strict accuracy of F1 while retaining the semantic benefits of F3, yielding the most balanced configuration for downstream FER.

Table 7. Ablation on supervision for geometric performance on BP4D test set. 3D errors are reported as mean \pm std, lower is better; CED AUC is shown with 3 decimals, higher is better; Best per column in **bold**.

Model	3D errors (mm) \downarrow		CED AUC \uparrow	
	Keypoints	Vertices	AUC@0.1	AUC@5.0
F0	98.9 \pm 29	0.1003 \pm 0.0294	0.426	0.981
F1	96.6\pm29	0.0993\pm0.0291	0.454	0.982
F2	97.7 \pm 29	0.0996 \pm 0.0292	0.435	0.982
F3	97.9 \pm 29	0.0998 \pm 0.0291	0.408	0.982
F4	97.7 \pm 29	0.0998 \pm 0.0292	0.444	0.982

Impact of Emotion Loss We vary the emotion-loss weight λ_{emo} in the encoder objective (Eq. (10)), where \mathcal{L}_{emo} is defined in Eq. (7), and evaluate both 3D geometry on BP4D (Tab. 8) and affect performance (Tab. 5).

Geometry is largely stable across λ_{emo} : AUC@5.0 remains 0.982 for all settings, vertex error fluctuates within ~ 0.001 mm, and keypoint/strict AUC@0.1 show only mild trade-offs (best keypoints at 0.5, best AUC@0.1 at 10). In contrast, affect metrics benefit from a stronger emotion signal: $\lambda_{\text{emo}} \in [5, 10]$ yields the top FER scores, with $\lambda_{\text{emo}}=5$ achieving the best F1 and V-CCC/RMSE, and $\lambda_{\text{emo}}=10$ slightly higher A-CCC/RMSE. Importantly, $\lambda_{\text{emo}}=5$ also minimizes FLAME parameter MSE for both $\{\psi_{\text{exp}}, \theta_{\text{jaw}}\}$ and β , indicating better magnitude calibration without geometric degradation. Overall, increasing λ_{emo} enhances affect alignment while keeping geometry essentially unchanged; $\lambda_{\text{emo}}=5$ provides the best balance used in our final model.

Table 8. Ablation on emotion-loss weight λ_{emo} for geometric performance on BP4D test set. 3D errors are reported as mean \pm std (lower is better); CED AUC is shown with 3 decimals (higher is better). Best per column in **bold**.

λ_{emo}	3D errors (mm) \downarrow		CED AUC \uparrow	
	Keypoints	Vertices	AUC@0.1	AUC@5.0
0.5	97.4 \pm 29	0.0994 \pm 0.0292	0.445	0.982
1	97.8 \pm 29	0.0998 \pm 0.0292	0.441	0.982
5	97.7 \pm 29	0.0998 \pm 0.0292	0.444	0.982
10	97.6 \pm 29	0.0992 \pm 0.0292	0.462	0.982

Fig. 11 shows reconstructions on AffectNet as the emotion weight increases left \rightarrow right ($\lambda_{\text{emo}} = 0.5, 1, 5, 10$). Small weights under-express (muted mouth opening and eyebrow motion); moderate weights ($\lambda_{\text{emo}} = 5$) yield class-consistent expressions with calibrated amplitudes; very large weight ($\lambda_{\text{emo}} = 10$) drives stronger activations (wider mouth/eyes, deeper nasolabial folds), which can look slightly exaggerated in some cases. This trend matches Tab. 8 and Tab. 5: geometry remains stable at coarse tolerance (AUC@5.0), strict local accuracy (AUC@0.1) peaks at higher λ_{emo} , while overall FER performance and perceived naturalness are best around $\lambda_{\text{emo}} = 5$.

8.3. Clustering Visualization Comparisons

We show the t-SNE and UMAP clustering visualization results of AffectNet val set for each 3D reconstruction methods in Fig. 14 and Fig. 15. The cross-method comparison shows that FIELDS yields the tightest, most separable class clusters with a smoother valence–arousal color gradient, indicating more discriminative—and more continuously affect-aligned—expression embeddings than EMOCA, SMIRK, or TEASER.



Figure 11. Visual examples on AffectNet. From left to right, original image, 3D face reconstruction via $\lambda_{\text{emo}} = 0.5, 1, 5, 10$.



Figure 12. BP4D 3D mesh model reconstruction examples (Female). From left to right: BP4D original image, 3D scan, fitted FLAME model, EMOCA[8], SMIRK[47], TEASER[34], FIELDS.



Figure 13. BP4D 3D mesh model reconstruction examples (Male). From left to right: BP4D original image, 3D scan, fitted FLAME model, EMOCA[8], SMIRK[47], TEASER[34], FIELDS.

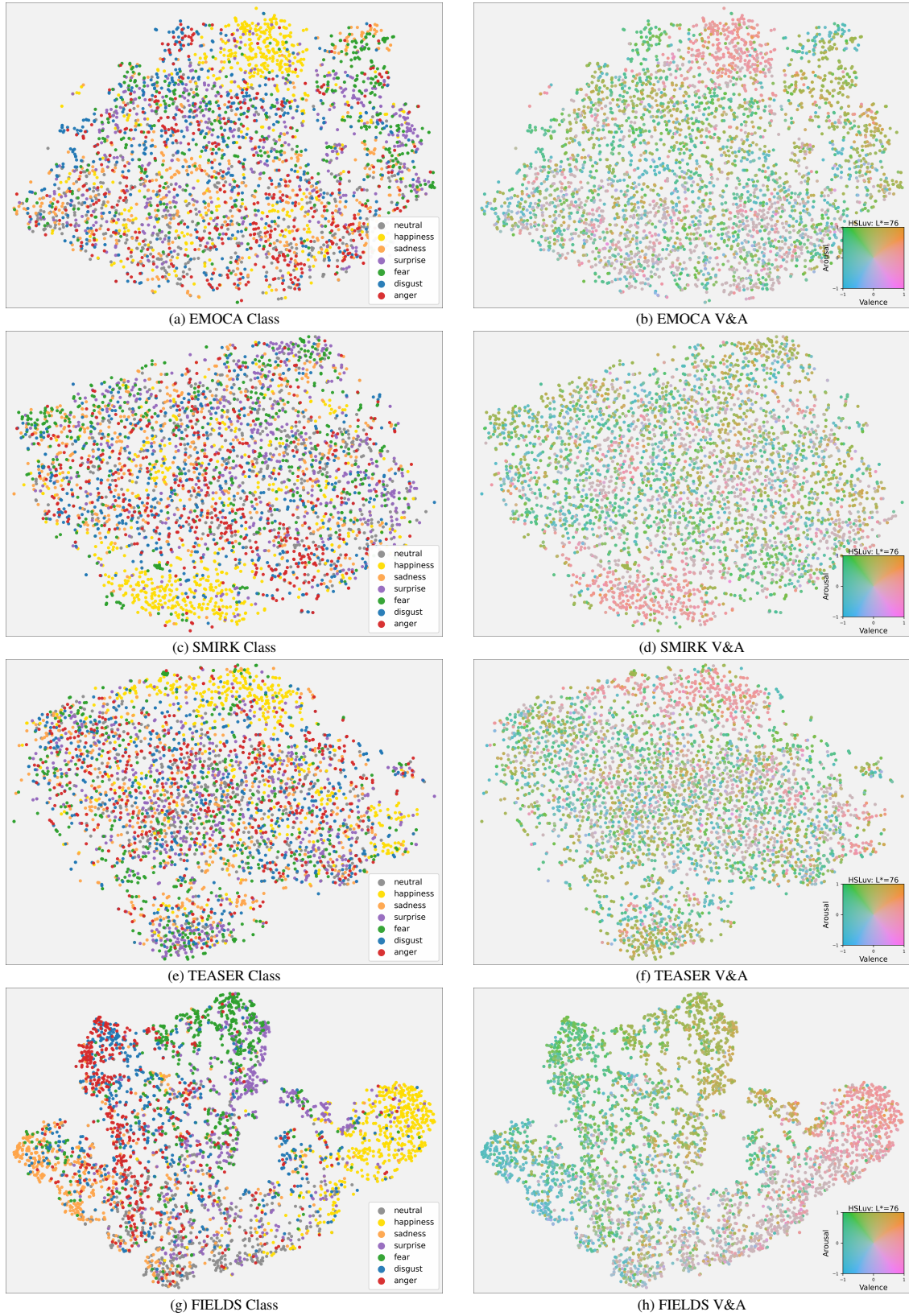


Figure 14. t-SNE Cluster Visualization of FLAME Expression Parameters.

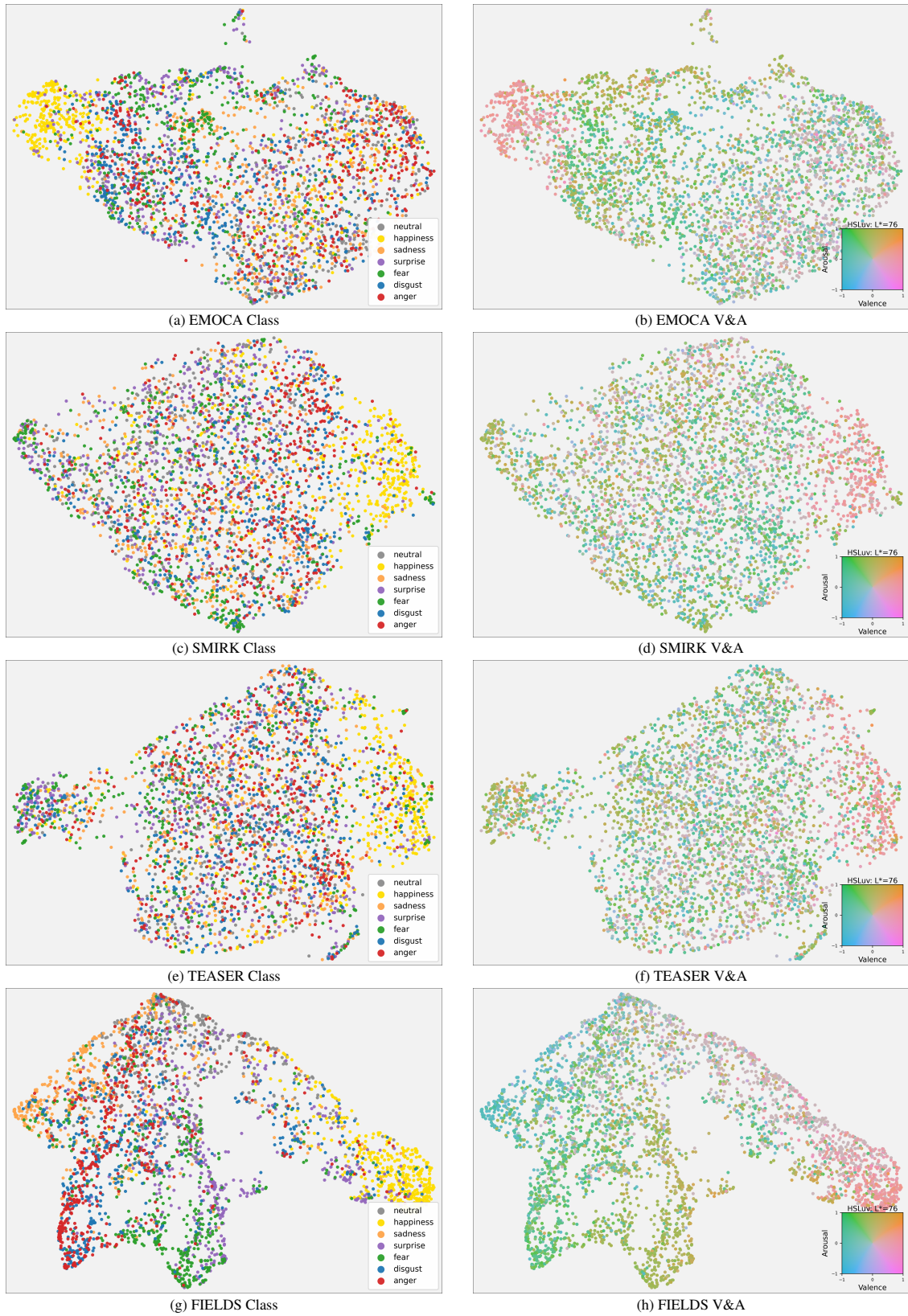


Figure 15. UMAP Cluster Visualization of FLAME Expression Parameters.